catalysts

MDPI

Article

Environmentally Friendly Fabrication of High-Efficient Fe-ZnO/Citric Acid-Modified Cellulose Composite and the Enhancement of Photocatalytic Activity in the Presence of H_2O_2

Agnieszka Fiszka Borzyszkowska [1,2,*], Agnieszka Sulowska [1], Ivar Zekker [3], Jakub Karczewski [4], Kai Bester [5] and Anna Zielińska-Jurek [1,2,*]

[1] Department of Processing Engineering and Chemical Technology, Gdansk University of Technology, Gabriela Narutowicza 11/12, 80-233 Gdansk, Poland
[2] EcoTech Center, Gdańsk University of Technology, G. Narutowicza 11/12, 80-233 Gdansk, Poland
[3] Institute of Chemistry, University of Tartu, 14a Ravila St., 50411 Tartu, Estonia
[4] Institute of Nanotechnology and Materials Engineering, Faculty of Applied Physics and Mathematics, Gdańsk University of Technology, Gabriela Narutowicza 11/12, 80-233 Gdansk, Poland
[5] Environmental Science, Århus University, Frederiksborgsvej 399, 4000 Roskilde, Denmark
* Correspondence: agnieszka.borzyszkowska@pg.edu.pl (A.F.B.); annjurek@pg.edu.pl (A.Z.-J.)

Citation: Fiszka Borzyszkowska, A.; Sulowska, A.; Zekker, I.; Karczewski, J.; Bester, K.; Zielińska-Jurek, A. Environmentally Friendly Fabrication of High-Efficient Fe-ZnO/Citric Acid-Modified Cellulose Composite and the Enhancement of Photocatalytic Activity in the Presence of H_2O_2. *Catalysts* **2022**, *12*, 1370. https://doi.org/10.3390/catal12111370

Academic Editors: Detlef W. Bahnemann, Wonyong Choi, Ioannis Konstantinou, Ewa Kowalska, Magdalena Janus and Vincenzo Vaiano, Zhi Jiang

Received: 31 August 2022
Accepted: 21 October 2022
Published: 4 November 2022

Abstract: In the present study, a novel Fe-ZnO/citric acid-modified cellulose composite (x%Fe-ZnO-y%CAC) was synthesized using an environmentally friendly hydrothermal method. The obtained samples were characterized by X-ray diffraction (XRD), scanning electron microscopy (SEM), UV−vis diffuse reflectance spectroscopy (DRS), Fourier transform infrared spectroscopy (FTIR), nitrogen physisorption, and electrochemical and photocurrent density analyses. The influence of the additives from the series of x%Fe-ZnO-y%CAC photocatalysts with Fe content from 0 to 5% and CAC content from 0 to 80% on photocatalytic degradation of ibuprofen (IBU) under simulated solar light was investigated. The photocatalyst 0.5%Fe-ZnO-40%CAC showed high photocatalytic activity of 0.0632 min^{-1} first-order kinetic rate constant and 46% TOC reduction of IBU under simulated solar light irradiation. Additionally, H_2O_2-assisted photocatalytic process was investigated for facilitating the IBU degradation in the presence of 0.5%Fe-ZnO-40%CAC; the first-order kinetic rate constant was 2.7 times higher compared to the process without addition of H_2O_2. Moreover, the effect of radical scavengers was examined to explain the degradation mechanism of IBU by synthesized photocatalysts supported with H_2O_2. The demonstrated system provides a low-cost and green approach to improve the photocatalytic activity of x%Fe-ZnO-y%CAC photocatalysts.

Keywords: photocatalysis; ZnO; cellulose; advanced oxidation processes; composites

1. Introduction

The dynamic development of industry and urbanization causes the presence of xenobiotics from the group of active pharmaceutical ingredients (API) in the aquatic environment, which are not susceptible to biological decomposition [1–4]. Some of the commonly used non-steroidal pain relievers and anti-inflammatory drugs (NSAIDs) are detected in various water bodies, especially in municipal wastewater, surface water, groundwater, freshwater, and sediments. NSAIDs bioaccumulate in living organisms, causing a toxic effect, which is a serious risk to all trophic levels in the food chain [5,6]. Particularly, ibuprofen (IBU) is the third most popular analgesic and anti-inflammatory drug in the world, and its toxic effects have been confirmed against many aquatic organisms, such as *Chlorella Vulgaris* and *Daphnia Magna* [6]. Therefore, work on the effective removal method facing organic micropollutants such as IBU is currently a worldwide challenge [7–9]. In this regard, the aim of this study was to investigate the possibility of

effective removal of IBU with the use of heterogeneous photocatalysis as a promising method for the improvement of wastewater treatment technology.

The photocatalysis process belongs to the group of advanced oxidation technologies (AOPs) that enable the decomposition and the mineralization of a broad group of micropollutants into nontoxic constituents [10,11]. AOPs include various techniques, for example, Fenton oxidation [12–14], catalytic ozonation [15,16] photocatalysis [17,18] and photo-Fenton oxidation [19]. In photocatalysis, among a variety of inorganic semiconductors applied as the photocatalyst, zinc oxide (ZnO) demonstrates good photocatalytic activity, high oxidation potential, and chemical and thermal stability. Despite a large band gap of ~3.37 eV, ZnO is several times cheaper than titanium(IV) oxide [20,21]. Its limitations, resulting from the absorption of UV radiation, are that it is prone to photocorrosion, and fast photorecombination of charge carriers, which can be overcome by introducing defects into the crystal structure of the semiconductor [22]. One of the simplest possible approaches to introduce defects into the crystal structure of the ZnO is doping with a transition metal, e.g., iron (Fe), which leads to an increase in visible light absorption [23]. Moreover, the Fe-doped photocatalyst can accelerate micropollutants removal in the presence of hydrogen peroxide (H_2O_2). According to this, the coupling of the photocatalytic process with the oxidation in the presence of external oxidants, such as H_2O_2, has also gained attention in the more efficient and rapid treatment of wastewater [24].

Following the assumptions of green chemistry, renewable materials could be applied to photocatalytic processes as biohybrids. In particular, cellulose-based materials, e.g., microcrystalline cellulose (CMC), nanocrystalline cellulose (CNC) and CAC are used to produce composites with a well-developed surface area to adsorb pollutants and improve the efficiency of photocatalytic degradation of pollutants [25,26]. According to Muhamed et al., the investigations for modification of photocatalysts as well as cellulose-based materials surfaces is required to tune the effectiveness of the photocatalysis. Moreover, cellulosic fibers can be easily functionalized in order to better integrate them with the photocatalyst [25,27]. For example, Nasiri Khalil Abad et al. [28] concluded that the incorporation of Au-ZnO into the cellulose–acetate matrix increased the porosity and water contact angle of the nanocomposite, which had a beneficial effect on the photocatalytic activity during Eosin Y dye removal. Similarly, Tamaddon et al. [29] prepared a nanocomposite based on magnetic zinc ferrite and methylcellulose, which showed over 77% mineralization of metronidazole after 100 min of treatment under UV irradiation.

In this regard, new hybrid photocatalytic materials consisting of Fe-ZnO with citric acid-modified cellulose were obtained and used for IBU photodecomposition. Moreover, the effect of Fe modification and CAC presence on photocatalytic degradation of Fe-ZnO-CAC ternary composites under simulated solar light was investigated. The obtained materials were characterized by FTIR, SEM, XRD, UV–vis spectroscopy, XPS and nitrogen physisorption. Furthermore, electrochemical impedance spectroscopy and transient photocurrent response were analyzed to explain the mechanism of IBU photocatalytic degradation. This study presents the application of the green chemistry approach for photocatalytic wastewater purification technology.

2. Results and Discussion

2.1. Characterization

The optical behavior of the synthesized materials was investigated by UV–visible diffuse reflectance (UV–vis) spectroscopy, and the results are shown in Figure 1. A slight red shift in the range above 300 nm of absorption is observed for CAC compared with pristine CMC (Figure 1a). The CAC content in the 0.5%Fe-ZnO-y%CAC composite slightly increased the adsorption intensity in the range above 400 nm compared with 0.5%Fe-ZnO. The energy bandgaps of all the samples were calculated from the plot drawn between the absorption energy hν (eV) and $(\alpha h\nu)^{0.5}$ using Tauc's method [30]. The estimated band gap values of ZnO and ZnO modified by Fe and CAC or CMC are presented in Table 1, and

Tauc plots of selected samples are shown in Figure S1 in the Supplementary Materials. Comparing the series of new synthesized x%Fe-ZnO-y%CAC composites, the sample 0.5%Fe-ZnO-40%CAC is characterized by the highest absorption intensity of light in the range above 400 nm, which indicates that the introduction of CAC and modification by Fe resulted in an enhanced light utilization efficiency. That was further evidenced by the photocatalytic degradation of IBU using x%Fe-ZnO-y%CAC composites.

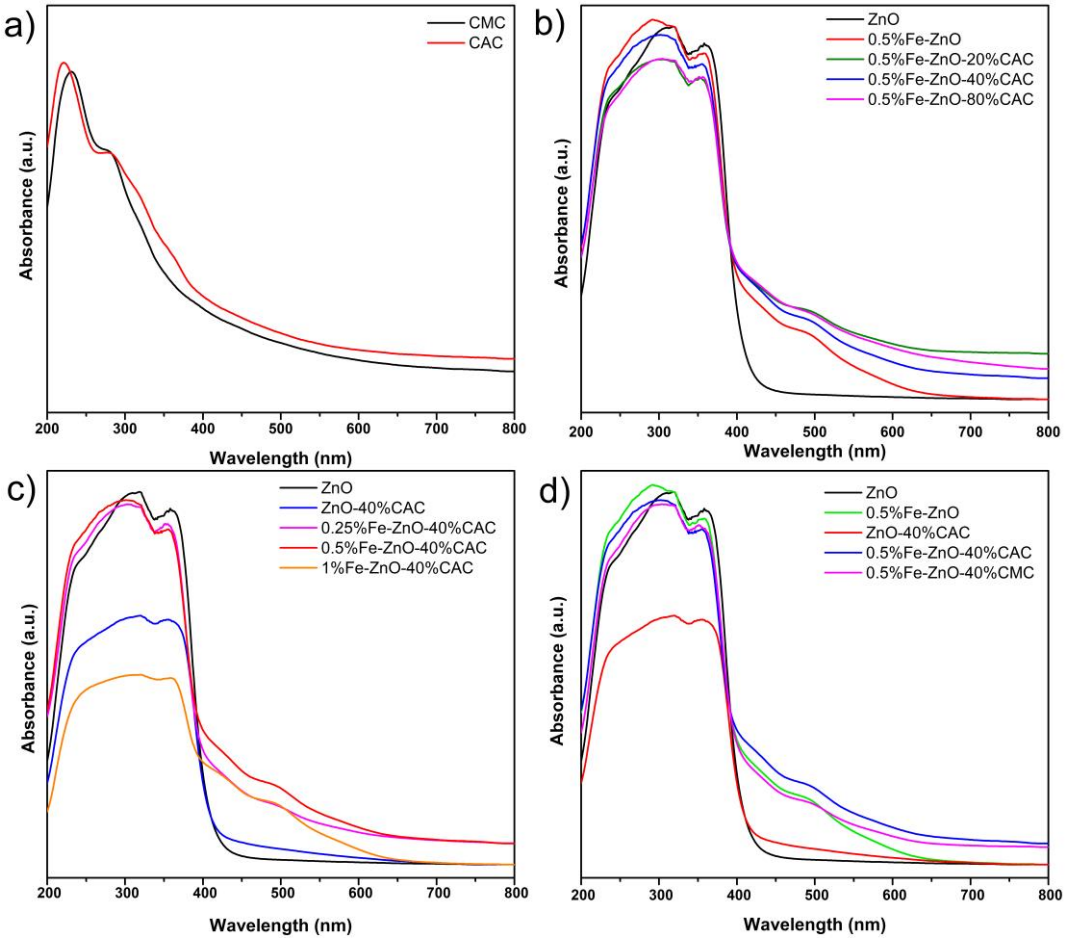

Figure 1. UV−vis diffuse reflectance spectra of the (**a**) purchased microcrystalline cellulose (CMC) and their citric acid modification (CAC); (**b**) composites with different CAC content; (**c**) composites with different Fe content; (**d**) composites with 0.5% Fe and/or 40% CAC.

The specific surface area of synthesized materials was measured by the physical adsorption/desorption of N_2. The values of BET surface area are presented in Table 1. The specific surface area was found to be 5.2, 5.2, 12.2 and 18.2 $m^2\ g^{-1}$ for ZnO, ZnO-40%CAC, 0.5%Fe-ZnO and 0.5%Fe-ZnO-40% CAC, respectively. The highest specific surface area of 20.6 $m^2\ g^{-1}$ was observed for the 1%Fe-ZnO-40%CAC composite. A high surface area would result in a greater surface able to withstand the photocatalytic reactions, thereby it may increase the photocatalytic activity of the composite material.

Table 1. Average crystallite size, lattice parameters (a = b (Å), c (Å), c/a ratio) and energy bandgap for hybrids from the series x%Fe-ZnO-y%CAC.

Sample Name	Fe Content (%)	CAC Content (%)	BET Surface Area (m^2 g^{-1})	Lattice Parameters			Eg (eV)
				a (Å)	b (Å)	c (Å)	
ZnO	0	0	5.2	3.252570	3.252570	5.210181	3.09
0.5%Fe-ZnO	0.5	0	12.2	3.251402	3.251402	5.205718	3.10
0.5%Fe-ZnO-20%CAC	0.5	20	14.6	3.252511	3.252511	5.210237	3.08
0.5%Fe-ZnO-40%CAC	0.5	40	18.2	3.254641	3.254641	5.210209	3.09
0.5%Fe-ZnO-80%CAC	0.5	80	18.5	3.253089	3.253089	5.209497	3.07
ZnO-40%CAC	0	40	5.0	3.247681	3.247681	5.201235	3.06
0.25%Fe-ZnO-40%CAC	0.25	40	16.5	3.244845	3.244845	5.194360	3.11
1%Fe-ZnO-40%CAC	1	40	20.6	3.240100	3.240100	5.186868	2.98
0.5%Fe-ZnO-40%CMC	0.5	40 (CMC)	10.0	3.250382	3.250382	5.205359	3.09

The chemical structure of obtained materials was analyzed by FTIR spectroscopy. In Figure 2, FTIR spectra of microcrystalline cellulose (CMC), citric acid-modified cellulose (CAC), 0.5%Fe-ZnO-40%CAC and ZnO-40%CAC are presented. The vibrations between 400 cm^{-1} and 590 cm^{-1} were attributed to the absorption band of zinc oxide (stretching of Zn−O) [31]. The characteristic peaks for cellulose are registered for both samples. A wide, large peak at 3347 cm^{-1} corresponds to the O-H stretching vibrations of hydroxyl groups. C-H symmetric stretching vibrations are recorded at 2901 cm^{-1} wavenumber. The peaks at 1431 cm^{-1} and 1371 cm^{-1} are assigned to C-H planar bending vibrations and C-H deformation vibrations, respectively. Other characteristic signals are found at 1318 cm^{-1} for CH_2 rocking deformations, 1164 cm^{-1} for C-O stretching vibrations or C-OH deformation and 1058 cm^{-1} for C–O–C pyranose ring vibrations. The signal at 897 cm^{-1} can be attributed to the C-H bending vibrations of β-glycosidic linkages of the glucose ring in the cellulose chain [32,33]. For CAC, an additional peak at 1729 cm^{-1} was recorded and is assigned to C=O stretching of ester or carboxylic functional groups. The presence of this signal is evidence of the functionalization of CMC with ester groups. Also, a new peak at wavenumber equaling to 1598 cm^{-1} is present, which can be ascribed to sodium citrate, which is built in cellulose chemical structure [34]. The CMC treatment with citric acid results in the esterification of hydroxyl groups in cellulose. All previously described peaks for citric acid-modified cellulose are registered for 0.5%Fe-ZnO-40%CAC and ZnO-40%CAC. The x%Fe-ZnO-y%CAC synthesis does not change the chemical structure of the citric acid-modified cellulosic material.

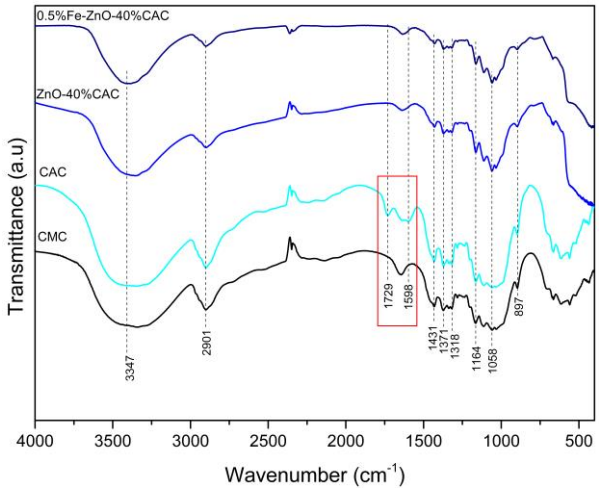

Figure 2. FTIR spectra of CMC, CAC, ZnO-40%CAC and 0.5%Fe-ZnO-40%CAC.

The results of morphological analysis of ZnO, CAC, CMC and ZnO modified by Fe and/or CAC are shown in Figure 3. Firstly, the modification of cellulose by citric acid did not cause significant changes in the morphology of this material. ZnO prepared by the hydrothermal method were rod-like particles, characterized by the non-uniform size, with two groups of dimensions, with smaller length of particles in the range from 200 to 500 nm and with the larger length in the range from 2 to 5 μm. During the hydrothermal synthesis in the presence of iron ions, rod-like particles of ZnO were also produced, with one group of dimensions in the range from 300 nm to 1 μm. Also, in this sample small particles were observed on ZnO with a diameter up to 50 nm. The synthesis of the composite ZnO-CAC resulted in the order of ZnO rod-like particles onto the shape of the flowers. Rod-like particles were characterized by different widths, with the narrow bars with a width of about 50 nm and wider rods becoming plates with the width up to 500 nm. The length of the narrow and wide particles was similar and equal from 1 to 3 μm. The most diverse structure was observed for the sample 0.5%Fe-ZnO-40%CAC, which consisted of rods with length from 500 nm up to 1.2 μm and smaller particles with the diameter of about 10 nm. It is also worth mentioning that the ZnO particles were directly coated onto the cellulose surface and therefore cellulose was not visible on the SEM images.

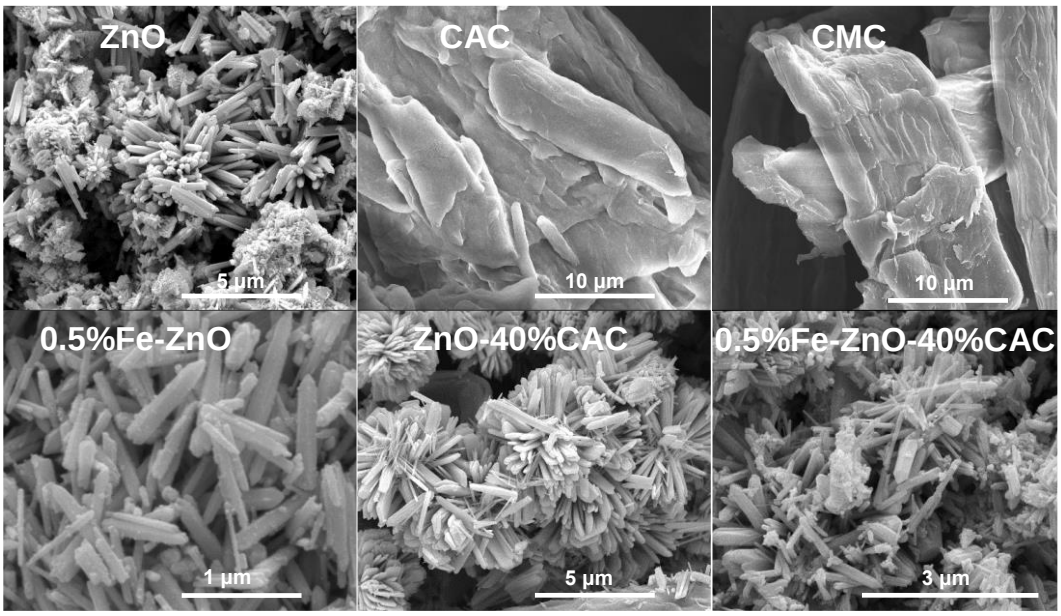

Figure 3. SEM images of selected materials.

The EDX analysis of the prepared x%Fe-ZnO-40%CAC were performed to identify their elemental composition. In Table 2, there are presented EDX analysis results on element composition in photocatalysts consisting of O, Zn and Fe elemental peaks. Any other signals from other elements were not noticed, indicating the high purity of the synthesized material. Carbon tape was used for holding the analyzed sample during EDX measurement, and for this reason, signals of presented C element were removed. Composites also contained carbon due to the fact that 40% of the content of catalysts was CAC, which consisted of about 44 weight % C. According to the correction for the carbon presence in the composites, the percentage of Fe was assumed as 0.42, 0.64 and 1.35 mol % for 0.25%Fe-ZnO-40%CAC, 0.5%Fe-ZnO-40%CAC and 1%Fe-ZnO-40%CAC, respectively. It is worth mentioning that the content of Fe was in good relation between the samples along with increasing content of Fe.

Table 2. EDX data for x%Fe-ZnO-40%CAC photocatalysts.

Sample Name	Element O mol %	Element Fe mol %	Element Zn mol %	
0.25%Fe-ZnO-40%CAC	51.4	0.6	48.0	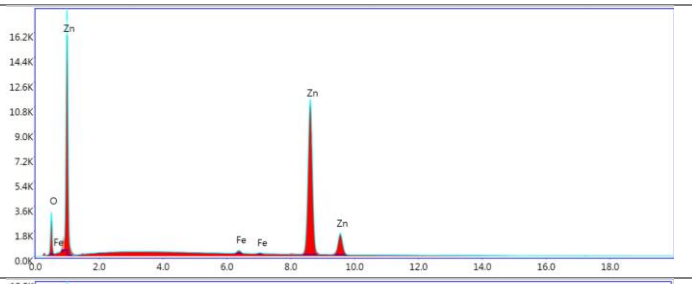
0.5%Fe-ZnO-40%CAC	53.2	0.9	45.8	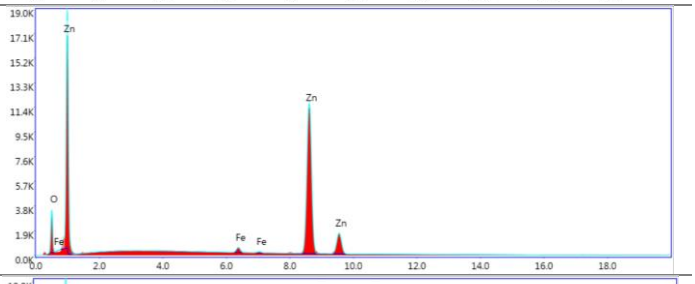
1%Fe-ZnO-40%CAC	51.4	1.9	46.7	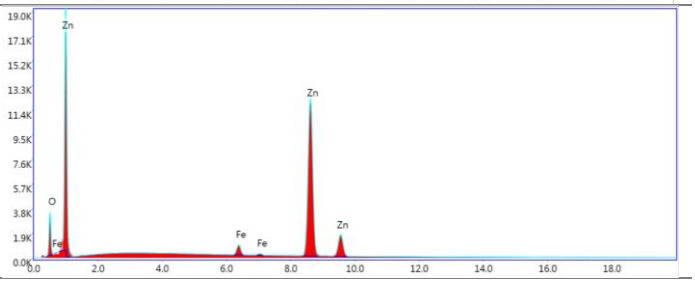

In Figure 4a, the diffraction pattern of CAC remained unchanged after the process of citric acid-catalyzed acetylation compared to the substrate CMC, suggesting that microcrystals maintained their original crystalline structure. It can be observed the broad diffraction peak at 2θ = 15.6°, sharp intense peak at 2θ = 21.8° and small peak at 2θ = 34.8° corresponding to the crystal planes (110 and 110), (200) and (004) of the cellulose, respectively. The crystallinity index of microcrystalline cellulose and citric acid-modified cellulose were 0.59 and 0.64, respectively. The XRD diffraction patterns of the ZnO and hybrids of ZnO modified by Fe and CAC or CMC are presented in Figure 4b. According to the standard JCPDS card no. 36-1454, all XRD peaks can be indexed to the wurtzite structure with S.G. P63mc (186) of ZnO based on the diffraction peaks and locations [35]. The peaks at 2θ of 31.9°, 34.6°, 36.4°, 47.7°, 56.8°, 63.0°, 66.4°, 67.9°, 69.1°, 72.5° and 76.9° correspond to the (100), (002), (101), (102), (110), (103), (200), (112), (201), (004) and (202) planes of ZnO with wurtzite structure. No other diffraction peaks arising from the Fe, CAC and/or CMC were detected in the XRD patterns of synthesized materials.

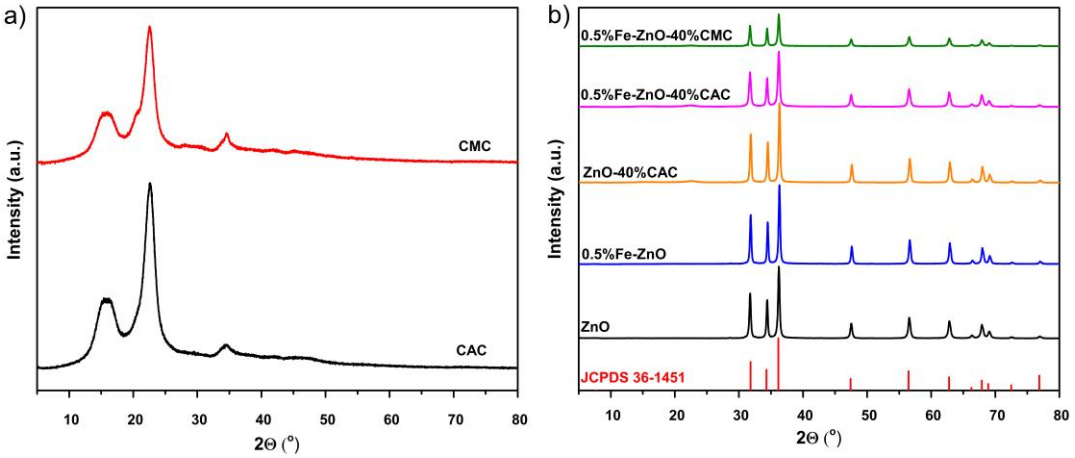

Figure 4. XRD patterns of the (**a**) purchased microcrystalline cellulose (CMC) and their citric acid modification (CAC); (**b**) ZnO-based composites with 0.5% Fe and/or 40% cellulose.

X-ray photoelectron spectroscopy (XPS) is an effective analytical method for studying elemental composition, types of functional groups and chemical bonds present on the surface of solids. The XPS analysis of 0.5%Fe-ZnO-40%CMC sample was performed and the results are presented in Figure 5. Based on the XPS spectra presented in Figure 5a, it was shown that the analyzed sample consisted of Zn, C and O atoms in 21.6, 28.8 and 49.6%, respectively. Signals for Fe were not registered during XPS analysis, which indicates that Fe was below the detection limit or introduced into the structure of ZnO. In Figure 5b, a peak at a binding energy of 1021.7 eV corresponds to Zn^{2+} of ZnO [36]. In Figure 5c, the XPS spectrum of the C 1s region presents an asymmetric peak. This indicated the presence of carbon in different oxidation states. The curve was fitted to four distinct carbon components: (i) C 1s A at 284.7 eV is attributed to C-C bonds in 67.83 at. %; (ii) C 1s B at 286.2 eV is a signal for C-O bonds and at. % concentration equals 17.43%; (iii) C 1s C at 287.6 eV is for C=O bonds and the concentration is 3.4 at. %; (iv) C 1s D at a binding energy of 288.7 eV corresponds to carbon in O=C-O bonds; at. % of this signal is 11.34% [37]. Also, an asymmetric peak for O 1s was registered (see Figure 5d) and three different signals were distinguished at: 530.28 eV, 531.68 eV and 532.77 eV, which can be assigned to oxygen in Zn-O, C=O and C-O bonds, respectively [36,37].

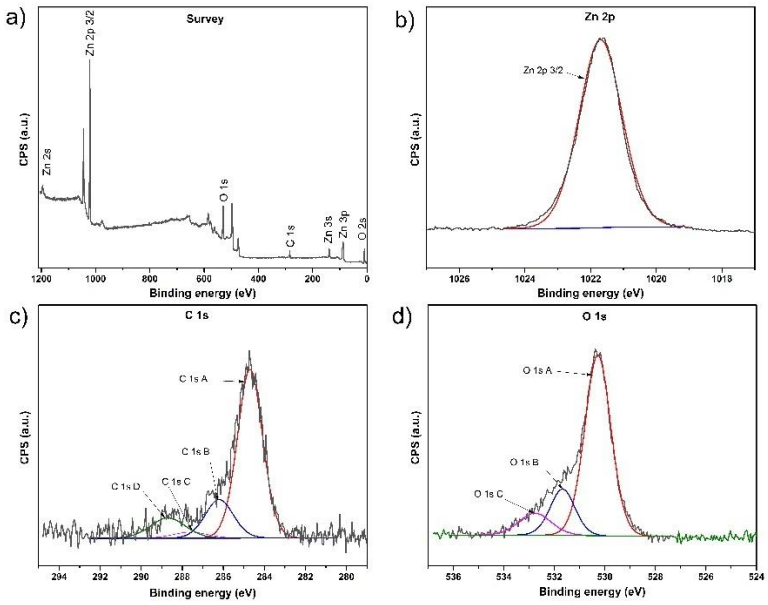

Figure 5. X-ray photoelectron spectroscopy spectra of 0.5%Fe-ZnO-40%CAC: (**a**) survey spectra, (**b**) Zn 2p spectra, (**c**) C 1s spectra, (**d**) O 1s spectra.

The electrochemical impedance spectroscopy (EIS) was performed in an aqueous electrolyte solution of 1 M Na_2SO_4 at ambient temperature (25 °C). Results of this analysis for ZnO, 0.5%Fe-ZnO, ZnO-40%CAC, 0.5%Fe-ZnO-40%CAC and 0.5%Fe-ZnO-40%CMC are presented in Figure 6. The arcs on the spectrogram of EIS electrochemical impedance indicate the resistance of the charge transfer layer at the interface between the electrode and electrolyte. Higher efficiency of charge transfer is revealed by a smaller arc, which indicates a lower resistance [38]. In our study, the smallest arc radius was observed for the 0.5%Fe-ZnO-40%CAC composite, which implies that the charge transfer layer resistance of this material was smaller than for other measured photocatalysts: ZnO, 0.5%Fe-ZnO and ZnO-40%CAC. It was observed that the presence of CAC caused a higher efficiency of charge transfer compared to the composite with non-modified microcrystalline cellulose. Additionally, every applied modification of ZnO accelerated the photocatalytic activity due to better separation of the photo-induced electron-hole pairs indicated by exhibiting better transfer efficiency.

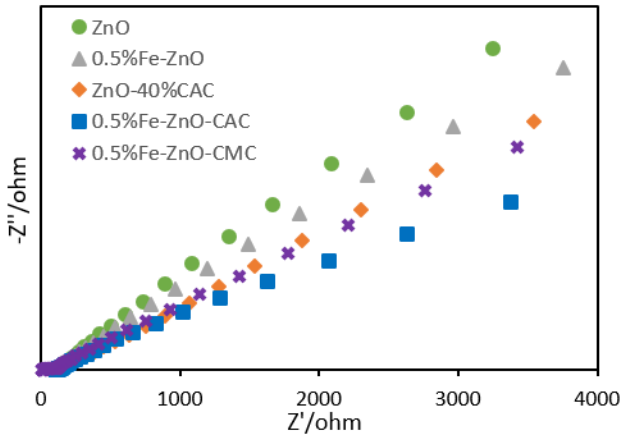

Figure 6. Electrochemical impedance spectroscopy measurement of the 0.5%Fe-ZnO-40%CAC and 0.5%Fe-ZnO-40%CMC ([Na_2SO_4] = 1 M).

Furthermore, the photocurrent responses of ZnO modified with Fe and/or CAC were performed to study the separation and transfer efficiency of photogenerated charge carriers in the photocatalysts. This measurement was performed in five on–off cycles of LED light irradiation in the range from 380 to 390 nm. As shown in Figure 7, when the light is turned on, immediate photocurrent responses can be observed. The 0.5%Fe-ZnO photocatalyst exhibited the highest photocurrent density in comparison with other materials, which indicated the reduced interface resistance and the improved separation and migration efficiency of the photogenerated e/h^+ pairs. After several successive switch on–off cycles, the photocurrent results of ZnO and 0.5%Fe-ZnO decreased by about 16% and 18%, respectively. The modification of 0.5%Fe-ZnO by CAC decreased the photocurrent response but increased the stability of the following switching cycles and was lower in the last cycle only by 4%. Comparing the influence of cellulose modification by citric acid in the composite, the photocurrent was higher at about 50% for the sample 0.5%Fe-ZnO-40%CAC than for the sample 0.5%Fe-ZnO-40%CMC. Considering the trends of green materials, modification by CAC caused a significant increase in photocurrent response and affected positively on the stability of the 0.5%Fe-ZnO-40%CAC composite compared with the hybrid with CMC, so the operation of CMC modification by citric acid is reasonable.

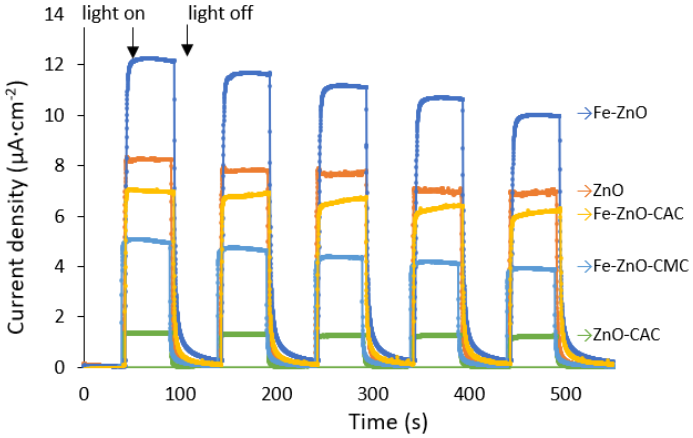

Figure 7. Transient photocurrent response of photocatalysts from 0.5%Fe-ZnO-40%CAC series (λ = 380–390 nm, [Na_2SO_4] = 1 M).

2.2. Photocatalytic Degradation of Ibuprofen

Firstly, the adsorption test was performed in the dark to determine the time necessary to achieve an equilibrium state before the initiation of the photocatalytic reaction. The process of IBU adsorption was negligible, with only less than 5% adsorbed on each synthesized photocatalyst within half an hour. Further dark adsorption process did not cause reducing the IBU concentration; therefore, adsorption–desorption equilibrium was achieved. Additionally, the photolysis process of IBU was investigated, occurring in the irradiation experiment parameters. The low oxidation rate by the direct photolysis system was observed, and the pseudo-first order kinetic rate constant (k) was low (k = 0.0011 min^{-1}), which is in accordance with other studies [39,40].

The photocatalytic activity of obtained samples was assessed by IBU degradation under simulated solar irradiation. The effect of the Fe and CAC content in the composites for IBU removal was investigated, and the results are summarized in Figure 8. According to Figure 8a, the increase of Fe content in the range of 0–0.5% in the x%Fe-ZnO-40%CAC composites resulted in an increase of the pseudo-first order reaction rate constant and TOC reduction efficiency. A further increase in the content of Fe caused a slight decrease in the rate constant; however, the mineralization of the pharmaceutical decreased but was still higher than for the composite without Fe. The highest removal efficiency was obtained for the composite ZnO-40%CAC with 0.5% of Fe, which is considered optimal Fe loading and selected for the detailed studies.

Figure 8b presents a dependence of CAC content on photocatalytic activity for samples with the constant amount of Fe in the composites equaling 0.5%. There is no significant difference in the IBU mineralization and the reaction rate constant for photocatalysts without CAC and with 20% of CAC. The content of CAC equal to 40% in the composite caused the improvement of photocatalytic properties. The degradation rate constant and mineralization increased by almost 20% and 8%, respectively, compared to the 0.5%Fe-ZnO-20%CAC sample. The further increase of CAC content up to 80% CAC was affected by lower photocatalytic activity observed by the reduction of the rate constant as well as by the lower TOC reduction. These results indicate that 40% of CAC is an optimal amount in the ternary 0.5%Fe-ZnO-y%CAC nanocomposites.

The effect of individual variable parameters, including 0.5%Fe and/or 40% CAC, as well as non-modified CMC on photocatalytic activity, is presented in the Figure 8c. Comparison includes the following samples: ZnO, ZnO-40%CAC, 0.5%Fe-ZnO, 0.5%Fe-ZnO-40%CAC and 0.5%Fe-ZnO-40%CMC. Among all mentioned materials, 0.5%Fe-ZnO-40%CAC possesses the highest rate constant and TOC reduction. It is worth emphasizing that the ternary composite with CAC is characterized by an improved rate constant and IBU mineralization measured as a TOC reduction compared to the sample with microcrystalline cellulose. The results demonstrate that cellulose modification by citric acid

treatment was reasonable and had a positive impact on IBU removal from aqueous solution under simulated solar light irradiation.

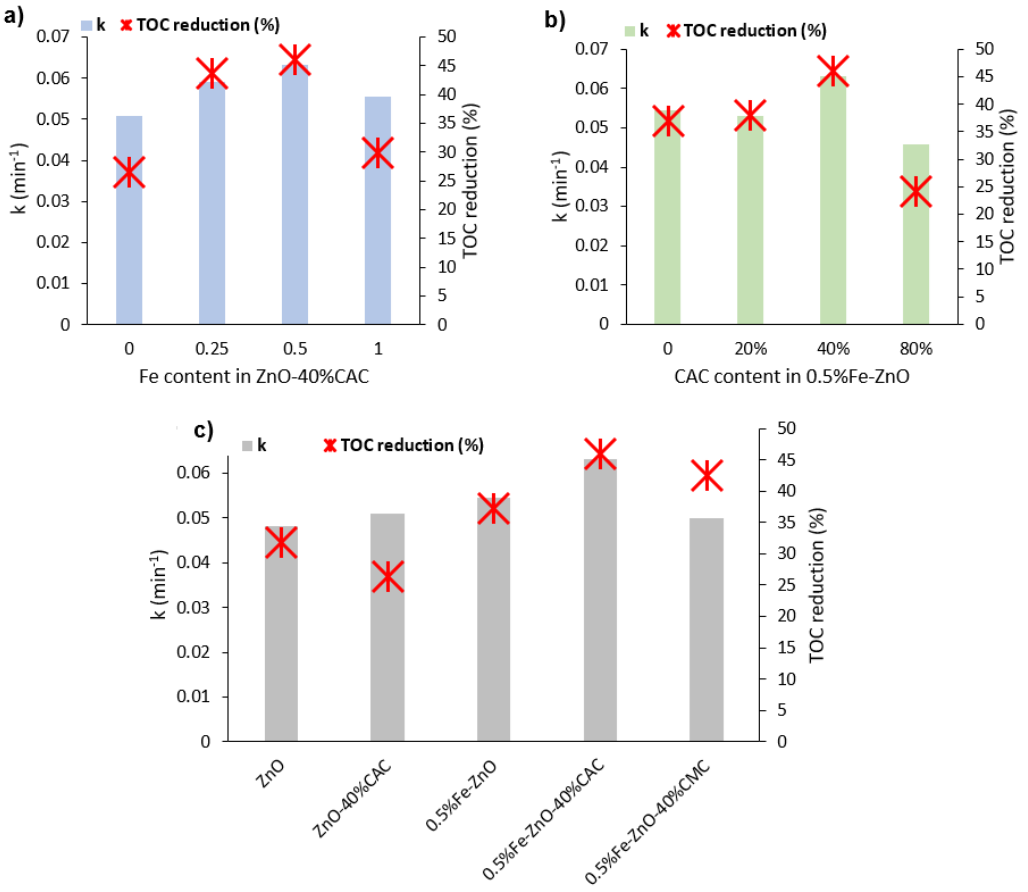

Figure 8. Comparison of degradation rate and mineralization of ibuprofen in the presence of different types of photocatalyst depending on (**a**) the Fe content in ZnO-40%CAC, (**b**) CAC content in 0.5%Fe-ZnO, (**c**) modification by 0.5%Fe and/or 40%CAC or 40%CMC of ZnO. Experimental conditions: IBU initial conc.: 20 mg dm^{-3}, V = 15 cm^3, photocatalyst: 0.5 g dm^{-3}, irradiation time = 120 min.

The photocatalytic efficiency of ibuprofen degradation in the presence of x%Fe-ZnO-y%CAC composites was compared to other types of photocatalysts already presented in the literature for IBU photocatalytic degradation (see in Table S2). For the commercial P25 TiO_2 photocatalyst irradiated using UV LED light source, Jallouli et al. [41] reported 100% degradation of IBU (60 mg·dm^{-3}) within 90 min. Another commercial TiO_2 from the Vetec company allowed for 100% degradation of IBU (10^{-4} mol·dm^{-3}) after 10 min of UV irradiation using a mercury lamp [42]. Also, ZnO-based photocatalysts were applied for IBU degradation, but the complete degradation of IBU was not achieved [40,43]. Relatively high photocatalytic activity of commercial BiOCl was reported by Arthur et al. [44] with the use of UV light, where 100% of IBU (20 mg·dm^{-3}) degradation was noticed after 20 min. Shibu et al. [45] synthesized α-Fe_2O_3/rGO nanocomposite and demonstrated 100% of IBU degradation when exposed to white LED light within 140 min but with the dose of photocatalysts 10 times higher than in our study. Fe_3O_4/Bi_2WO_6 nanohybrid was also used for IBU (10 mg·dm^{-3}) degradation under solar light, and these conditions allowed for 80% degradation within 120 min. Rosman et al. [46] fabricated PVDF membranes incorporated with ZnO/Ag_2CO_3/Ag_2O and used for IBU removal by membrane filtration and photocatalysis, which allowed for maximum 35.27% efficiency of this process.

2.2.1. Effect of H_2O_2

The process of photo-assisted peroxidation of IBU was evaluated for selected photocatalysts. The addition of H_2O_2 aims to increase the effectiveness of degradation of the target contaminants through accelerating oxidation by •OH radicals generated during photolytic cleavage of the H_2O_2 molecule (Equation (1)) [47]. Additionally, H_2O_2 can undergo reactions with generated species during the photocatalytic process, such as $O_2^{\bullet-}$ (Equation (2)) and e^- (Equation (3)), facilitating the degradation of pollutants.

$$H_2O_2 + h\upsilon \rightarrow 2\ {}^{\bullet}OH \quad (1)$$

$$H_2O_2 + O_2^{\bullet-} \rightarrow {}^{\bullet}OH + OH^- + O_2 \quad (2)$$

$$H_2O_2 + e^- \rightarrow {}^{\bullet}OH + OH^- \quad (3)$$

The degradation of IBU under the H_2O_2-assisted photocatalytic processes in the presence of selected photocatalysts was investigated, and the results are presented in Figure 9. The degradation rate constant for pure ZnO was similar both with and without H_2O_2. The differences in photocatalytic activity depending on H_2O_2 were observed for Fe-containing photocatalysts. In the case of 0.5%Fe-ZnO, the rate constant increased from 0.060 min^{-1} without H_2O_2, to 0.089 min^{-1} in the presence of H_2O_2. Also, for this sample IBU mineralization increased from 37% to 54% without and with H_2O_2, respectively. Moreover, the greatest enhancement of IBU removal was observed for the 0.5%Fe-ZnO-40%CAC photocatalyst, which was characterized by three times higher rate constant with H_2O_2 addition in comparison to the process without a supporting oxidant.

Additionally, the electric energy per order values were calculated to determine the energy efficiency of UV-based AOPs. The electrical energy per order was calculated according to the Equation (4):

$$E_{EO} = \frac{P_{el} \cdot t}{V \cdot \log\left(\frac{C_0}{C}\right)}, \quad (4)$$

where P_{el} is the rated power per reactor (in W), t is the irradiation time (in hours), V is the volume of effluent taken (in dm^3), and C_0 and C are the concentrations (in $mg \cdot dm^{-3}$) at initial and after t time [48]. Calculated electric energy per order values are presented in Table S1. They clearly proved that in the presence of Fe-ZnO/citric acid-modified cellulose composite, the energy consumption is reduced by 30% during the photocatalytic process compared with ZnO material. Moreover, H_2O_2-assisted processes in the presence of modified samples significantly reduced electric energy per order up to 2.6 times for the 0.5%Fe-ZnO-40%CAC sample. The effect of iron presence in the sample during H_2O_2-assisted processes was the most influencing. This shows the significance that the H_2O_2-assisted process in the presence of newly synthesized 0.5%Fe-ZnO-40%CAC composite is reasonable for future photocatalytic water treatment due to the improved efficiency when compared to the process in the presence of ZnO.

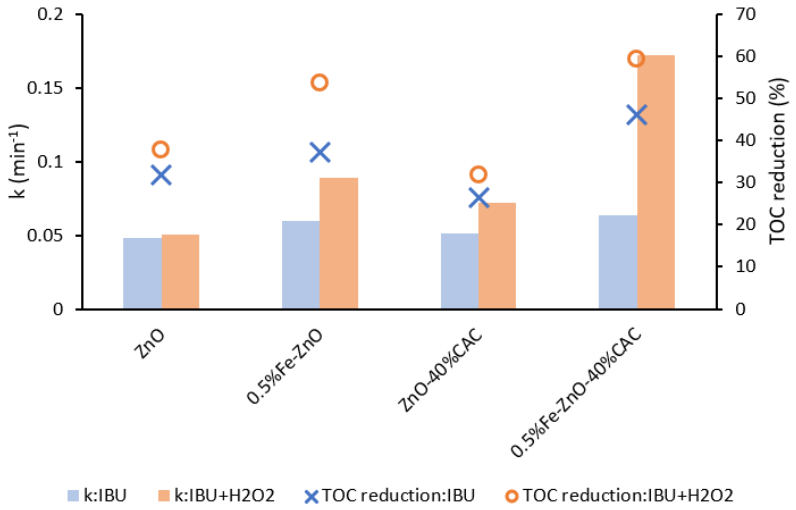

Figure 9. Comparison of degradation rate and mineralization of ibuprofen in the presence of different types of photocatalyst in the absence and presence of hydrogen peroxide. Experimental conditions: IBU initial conc.: 20 mg·dm^{-3}, H_2O_2 (5 mmol·dm^{-3}), V=15 cm^3, photocatalyst: 0.5 g·dm^{-3}, irradiation time=120 min.

2.2.2. Analyses of Reactive Oxygen Species

Generally, hydroxyl radicals, superoxide anion radicals and holes are the reactive oxygen species that cause micropollutants degradation in photocatalytic processes. To study the role of reactive species isopropyl alcohol (IPA), ammonium oxalate (AO) and para-benzoquinone (BQ) were used in this experiment to trap •OH, h^+, and $O_2^{\bullet-}$, respectively [49].

The first-order kinetic rate constant changes when the individual scavengers are applied (Figure 10). The degradation of IBU using 0.5%Fe-ZnO-40%CAC decreased in the presence of every applied scavenger during the photocatalytic process and also during photocatalytic process assisted with H_2O_2. The IBU degradation was mainly influenced by $O_2^{\bullet-}$ species [50]. The h^+ (holes) plays a secondary role, whereas the contribution of hydroxyl radicals in the degradation is not remarkable. It is worth emphasizing that the degradation of IBU in the presence of ZnO and ZnO-40%CAC assisted by H_2O_2 was not inhibited and even accelerated in the case of ZnO with IPA and AO, as well as ZnO-40%CAC with IPA. This phenomenon can be explained by the decomposition of H_2O_2 on photocatalysts either by reduction (Reaction 5) or oxidation (Reaction 6):

$$H_2O_2 + 2\,e^- + 2\,H^+ \rightarrow 2\,H_2O \quad (5)$$

$$H_2O_2 + 2\,h^+ \rightarrow O_2 + 2\,H^+ \quad (6)$$

The generation of e^- and h^+ species can cause the decomposition of H_2O_2 into water and oxygen molecules [51]. In the case of the experiments performed in the present study, the reason for accelerating reactions was the trapping of holes and, consequently, the inhibition of the five and six reactions. The non-consumed H_2O_2 by holes could then positively influence the reaction rate constant, causing the possibilities of reactions with the action of H_2O_2 as well as resulting in the inhibition of charge carriers' recombination [52]:

$$H_2O_2 + e^- \rightarrow {}^{\bullet}OH + OH^- \quad (7)$$

$$H_2O_2 + O_2^{\bullet-} \rightarrow {}^{\bullet}OH + OH^- + O_2 \quad (8)$$

Photocatalysts containing Fe produced all studied species, which was positively reflected by their photocatalytic activity. The degradation in the presence of composites with Fe can be enhanced due to the synergistic effect between the photocatalyst and photo-Fenton process [53], as shown in the following equations:

$$Fe^{3+} + e^{-} + h\upsilon \rightarrow Fe^{2+} \quad (9)$$

$$Fe^{2+} + O_2 \rightarrow Fe^{3+} + O_2^{\bullet-} \quad (10)$$

$$Fe^{3+} + H_2O + h\upsilon \rightarrow Fe^{2+} + H^+ + {}^{\bullet}OH \quad (11)$$

According to the obtained results, $^{\bullet}OH$ and $O_2^{\bullet-}$ are the major ROS responsible for efficient photodegradation in the presence of 0.5%Fe-ZnO assisted by H_2O_2. However, during the photodegradation in the presence of 0.5%Fe-ZnO-40%CAC/H_2O_2, $O_2^{\bullet-}$ became the major ROS.

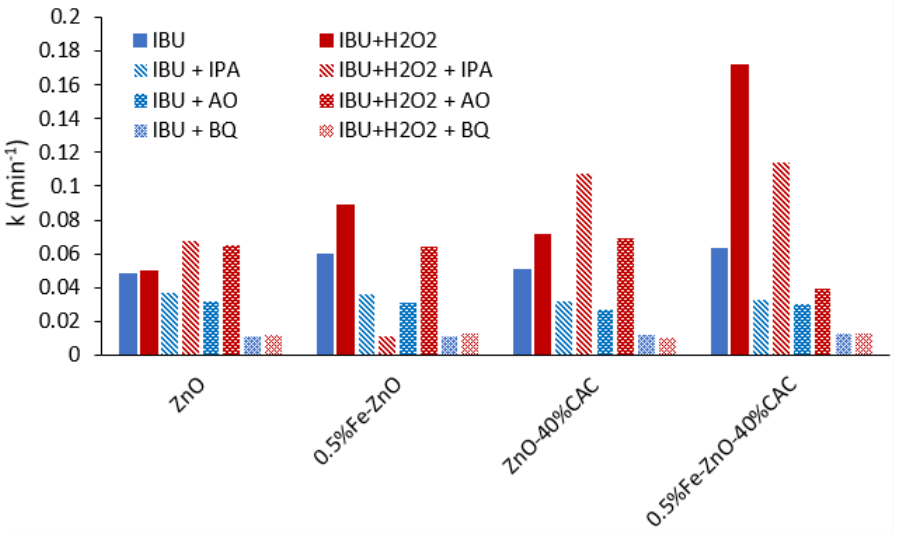

Figure 10. Effect of scavengers on photocatalytic degradation using ZnO, 0.5%Fe-ZnO, ZnO-40%CAC and 0.5%Fe-ZnO-40%CAC on the first-order kinetic rate constant in the presence of isopropanol (IPA) and ammonium oxalate (AO) and benzoquinone (BQ).

2.2.3. Stability of the Photocatalysts

Furthermore, the stability of ZnO and 0.5%Fe-ZnO-40%CAC was confirmed in the subsequent photocatalytic cycles of degradation with and without H_2O_2 addition, as shown in Figure 11. Sample ZnO and 0.5%Fe-ZnO-40%CAC, after three cycles of photodegradation, maintained photocatalytic stability, but a slight reduction of TOC reduction was observed after the third cycle in the presence of 0.5%Fe-ZnO-40%CAC. On the other hand, after three subsequent photocatalytic processes coupled with H_2O_2, the degradation rate slightly decreased. Nevertheless, the photocatalytic degradation efficiency of 0.5%Fe-ZnO-40%CAC/H_2O_2 was still remarkably improved compared to the degradation processes of ZnO and ZnO/H_2O_2 samples.

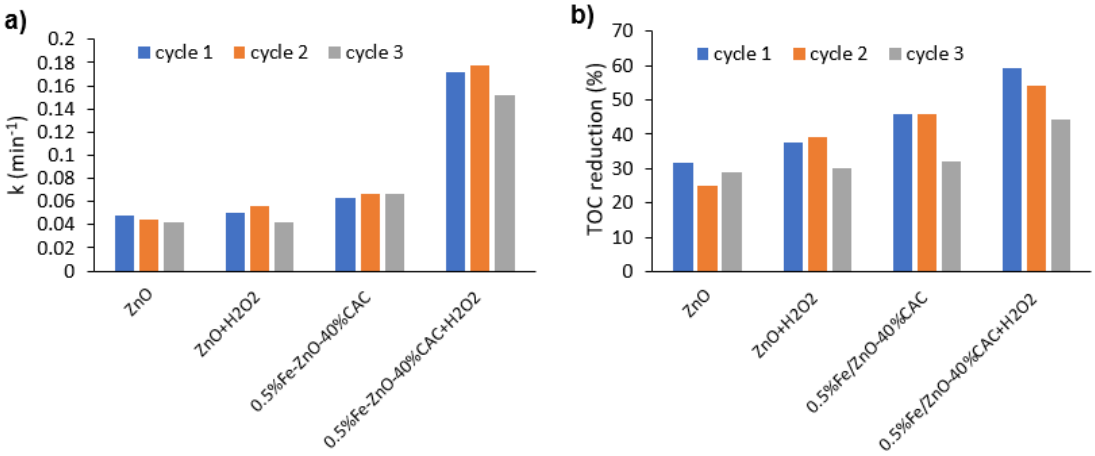

Figure 11. Ibuprofen photocatalytic decomposition (**a**) and mineralization measured as TOC reduction (**b**) over ZnO, 0.5%Fe-ZnO-40%CAC and H_2O_2 during subsequent photodegradation cycles.

3. Materials and Methods

3.1. Experiment Materials

Zinc acetate dihydrate $(CH_3COO)_2Zn{\times}2H_2O$ analytical reagent grade was purchased from AppliChem (Germany), iron(III) nitrate nonahydrate ($Fe(NO_3)_3{\times}9H_2O$, 98%) and NiO (99.998%) were purchased from Alfa Aesar (USA), microcrystalline cellulose ($(C_6H_{10}O_5)_n$) was purchased from Chempur (Poland). Sodium hydroxide (NaOH, 99.9%), citric acid monohydrate ($C_6H_8O_7{\times}H_2O$, 99.9%), ammonia solution 25%, hydrochloric acid (HCl 34–37%), hydrogen peroxide (H_2O_2, 30%) and 2-propanol ($(CH_3)_2CHOH$, 99.9%) were all obtained from POCh (Poland). P-benzoquinone (98%) and ammonium oxalate monohydrate ($(NH_4)_2C_2O_4$, 99.5%) were provided by Sigma Aldrich. Acetonitrile (ACN, CH_3CN, LCMS grade) was obtained from Supelco, and orthophosphoric acid (H_3PO_4, with HPLC electrochemical grade) was obtained from Fisher Chemical (USA).

3.2. Synthesis of CAC

Cellulose was modified by one-pot synthesis route according to procedure proposed by Yu et al. [54]. Firstly, 8 g of microcrystalline cellulose was placed in a two-neck round-bottom flask with a volume of 500 cm^3. Then 400 cm^3 of mixed citric acid and hydrochloric acid (360 cm^3 of 3 M citric acid; 40 cm^3 of 6 M HCl) was added to the flask. A reaction of cellulose modification was performed at 80 °C for 8 h with a continuous magnetic stirring. Next, the mixture was cooled to room temperature and 25% ammonia solution was added to neutralize obtained citric acid-modified cellulose (CAC). The total volume of the final CAC solution was 900 cm^3.

3.3. Synthesis of Fe-ZnO/CAC Composites

The x% Fe–ZnO-y%CAC composites were prepared through the hydrothermal reaction proposed by Abdalkarim et al. [27] with minor modifications. In a typical procedure, 20 mmol of $(CH_3COO)_2Zn{\times}2H_2O$ was dissolved in 50 cm^3 of deionized water under magnetic stirring. Then, the designated amounts (0; 0.05; 0.1; and 0.2 mmol linked to 0; 0.25; 0.5 and 1 mole percent) of $Fe(NO_3)_3{\times}9H_2O$ was added to this solution and dissolved. Secondly, the amount of previously prepared CAC solution (0; 2.5; 5 and 10 cm^3, which linked to 0; 20; 40 and 80 wt%) was added. One sample was prepared with CMC (40 wt.%) instead of CAC to determine the influence of modification by citric acid. Next, NaOH (60 mmol; 2.4 g) dissolved in 50 cm^3 of deionized water was added to the solution and homogenized at room temperature under strong stirring. Afterwards, the suspension was transferred to a Teflon-lined stainless-steel autoclave and heated at a temperature of 80 °C for 16 h in an oven. Under these conditions, the series of x%Fe-ZnO-y%CAC hybrids were

obtained and washed several times with deionized water to neutral pH. Finally, photocatalysts were dried at 60 °C for 12 h.

3.4. Characterization

The morphology and X-ray energy dispersive spectroscopy (EDX) of the x%Fe-ZnO-y%CAC hybrids were characterized by FEI Quanta 250 FEG scanning electron microscope (Thermo Fisher Scientific Inc., USA). X-ray diffraction (Rigaku Intelligent X-ray diffraction system SmartLab, Japan) was used to analyze the crystal phase of the photocatalysts. Particle size was calculated using Debye–Scherrer equation: $D = \frac{K\lambda}{\beta cos\theta'}$, where K is the Scherrer constant, λ is wavelength of the X-ray beam used, β is the full width at half maximum of the peak and θ is the Bragg angle. Scherrer constant denotes the shape of the particle and its value for spherical crystals equaling to 0.94. The lattice parameters were calculated using PDXL2 software. The crystallinity index was determined based on the XRD measurement using an internal standard method with NiO, and Rietveld refinement was used [55]. Fourier transform infrared spectroscopy (FTIR) measurements (Nicolet iS10 FT-IR Spectrometer, Thermo Fisher Scientific Inc., MA, USA) were performed in the transmittance mode in the spectral range of 400–4000 cm−1. UV–visible light absorption spectra were collected using the UV–vis spectrophotometer (ThemoScientific Evolution 220) with the BaSO4 as a standard. Brunauer–Emmett–Teller (BET) surface area and pore size were measured using an ASAP 2020 physisorption analyzer (Micromeritics Instrument Co., Norcross, CA, USA). The electrochemical impedance spectroscopy (EIS) and transient photocurrent density for selected photocatalysts were measured using an Autolab PGSTAT204 potentiostat/galvanostat equipped with FRA32M module. Screen-printed carbon electrodes (DRP-110 type) were used during the electrochemical measurements. The photocatalyst layer was prepared by mixing 10 mg of sample, 1 cm^3 of deionized water and sonication of the suspension for 30 min in an ultrasound bath; next 10 μL of as-prepared suspension was pipetted onto a working electrode and dried at 30 °C . The measurements were performed in 1 M aqueous solution of sodium sulfate at ambient conditions. The X-ray photoelectron spectroscopic (XPS) measurements were performed using the UHV Prevac spectrometer with monochromatic Al Kα radiation (hn = 1486.6 eV) from an X-ray source operating at 10 kV. The Casa XPS software was used to evaluate the XPS data.

3.5. Photocatalytic Performance Measurements

The photocatalytic activities of hybrids from the series x%Fe-ZnO-y%CAC were evaluated in the photocatalytic degradations of ibuprofen (IBU) in an aqueous solution. In each experiment, 7.5 mg of a prepared photocatalyst was dispersed in 15 cm^3 of an aqueous solution of IBU (20 $mg \cdot dm^{-3}$). Prior to UV-vis light illumination, the suspension was magnetically stirred in the dark for 30 min to reach adsorption–desorption equilibrium. The light intensity was about 15 $mW \cdot cm^{-2}$, as measured with a UV radiometer (UV-B), and the temperature was maintained at 20 °C. Additionally, some processes were intensified by adding 5 $mmol \cdot dm^{-3}$ of H_2O_2 to the suspension at the beginning of irradiation. At a given time interval, the suspension solution was collected and filtered through syringe filters (φ = 0.2 μm) to measure IBU concentration and TOC was measured after every process. The concentrations of IBU were analyzed by high-performance liquid chromatography (HPLC; Shimadzu LC-20AD, Kyoto, Japan) equipped with a Phenomenex Kinetex C-18 column. An isocratic method set at a flow rate of 0.5 $cm^3 \cdot min^{-1}$ was used with the eluents consisting of an ACN/H_2O/H_3PO_4 phase with a ratio of 70/29.5/0.5 (v/v). Injection volume was 10 μL and the detection wavelength was 219 nm. Mineralization of the IBU was measured as a total organic carbon (TOC) reduction efficiency quantified using a carbon analyzer (Shimadzu TOC-L, Kyoto, Japan).

Additionally, the tests of stability were performed by using the most active composite material and the contribution of selected oxidants generated in photocatalysis was

examined. The contribution of $^{\bullet}OH$, h^{+} and $O_2^{\bullet-}$ was determined by conducting degradation processes of IBU in the presence of isopropanol -IPA (5 mmol dm^{-3}), ammonium oxalate-AO (5 mmol dm^{-3}) and benzoquinone -BQ (1 mmol dm^{-3}), respectively.

4. Conclusions

Novel Fe-ZnO-CAC ternary composites were successfully fabricated through an environmentally friendly and facile hydrothermal process. The effect of Fe content and CAC presence in the composite structure on photocatalytic degradation of IBU under simulated solar light was investigated. The optimal amount of Fe was 0.5 mol% Fe and CAC of 40 mol%. Based on FTIR and XRD analyses, the modification of cellulose by citric acid was confirmed, which resulted in the improvement of photocatalytic activity towards IBU degradation compared to the composite with microcrystalline cellulose.

The presence of CAC caused a higher efficiency of charge transfer compared to the composite with non-modified microcrystalline cellulose. Additionally, the modification of ZnO improved the photocatalytic activity due to better separation of the photo-induced electron-hole pairs. Sample 0.5%Fe-ZnO exhibited the highest photocurrent density. Detailed investigation of the reactive oxygen species confirmed the crucial role of $O_2^{\bullet-}$ during IBU photodegradation.

Additionally, the H_2O_2-assisted photocatalysis processes were performed, and the higher kinetic rate constant and mineralization measured as a TOC reduction was noticed for ternary composite compared with pure ZnO. The effect of Fe presence was indicated as the main reason for the higher efficiency of IBU degradation during the H_2O_2-assisted process. After subsequent cycles of degradation, the photocatalytic degradation efficiency of ibuprofen for 0.5%Fe-ZnO-40%CAC/H_2O_2 was markedly higher compared to ZnO and ZnO/H_2O_2 samples, confirming the positive effect of iron and cellulose modification by citric acid treatment in IBU removal from aqueous solution under simulated solar light.

Supplementary Materials: The following supporting information can be downloaded at: https://www.mdpi.com/article/10.3390/catal12111370/s1, Table S1: Examples of a current study of the photocatalytic IBU in degradation in the presence of different materials; Figure S1: Tauc plot of a) ZnO, b) 0.5%Fe-ZnO and c) 0.5%Fe-ZnO-40%CAC; Table S2: Electrical energy per order for IBU degradation in the presence of selected photocatalysts during photocatalytic process and supported with H_2O_2; Figure S2: Trend of first-order linearized equation used for the calculation of kinetic parameters of selected photocatalytic processes. References [40–46] are cited in the supplementary materials.

Author Contributions: Conceptualization, A.F.B. and A.Z.-J.; methodology, A.F.B., A.Z.-J. and A.S.; validation, A.F.B., A.Z.-J. and A.S.; formal analysis, A.F.B. and A.Z.-J.; investigation, A.F.B., A.S. and J.K.; resources, A.F.B.; writing—original draft preparation, A.F.B. and A.S.; writing—review and editing, A.F.B., A.Z.-J., A.S., I.Z. and K.B.; visualization, A.F.B. and A.S.; supervision, A.Z.-J., K.B.; I.Z.; funding acquisition, A.F.B. All authors have read and agreed to the published version of the manuscript.

Funding: Financial support of these studies from the Gdańsk University of Technology by the DEC-6/2021/IDUB/II. 2/Sc/035336 grant under the SCANDIUM-'Excellence Initiative-Research University' program is highly acknowledged.

Data Availability Statement: The authors confirm that the data supporting the findings of this study are available within the article. Derived data supporting the findings of this study are available on request.

Acknowledgments: Financial support of these studies from Gdańsk University of Technology by the DEC-6/2021/IDUB/II. 2/Sc/035336 grant under the SCANDIUM-'Excellence Initiative-Research University' program is gratefully acknowledged.

Conflicts of Interest: The authors declare no conflict of interest.

References

1. Patel, M.; Kumar, R.; Kishor, K.; Mlsna, T.; Pittman, C.U.; Mohan, D. Pharmaceuticals of emerging concern in aquatic systems: Chemistry, occurrence, effects, and removal methods. *Chem. Rev.* **2019**, *119*, 3510–3673. https://doi.org/10.1021/acs.chemrev.8b00299.
2. Tiwari, B.; Sellamuthu, B.; Ouarda, Y.; Drogui, P.; Tyagi, R.D.; Buelna, G. Review on fate and mechanism of removal of pharmaceutical pollutants from wastewater using biological approach. *Bioresour. Technol.* **2017**, *224*, 1–12. https://doi.org/10.1016/j.biortech.2016.11.042.
3. Wahab, M.; Zahoor, M.; Muhammad Salman, S.; Kamran, A.W.; Naz, S.; Burlakovs, J.; Kallistova, A.; Pimenov, N.; Zekker, I. Adsorption-membrane hybrid approach for the removal of azithromycin from water: An attempt to minimize drug resistance problem. *Water* **2021**, *13*, 1969. https://doi.org/10.3390/w13141969.
4. Comber, S.; Gardner, M.; Sörme, P.; Leverett, D.; Ellor, B. Active pharmaceutical ingredients entering the aquatic environment from wastewater treatment works: A cause for concern? *Sci. Total Environ.* **2018**, *613–614*, 538–547. https://doi.org/10.1016/j.scitotenv.2017.09.101.
5. Adeleye, A.S.; Xue, J.; Zhao, Y.; Taylor, A.A.; Zenobio, J.E.; Sun, Y.; Han, Z.; Salawu, O.A.; Zhu, Y. Abundance, fate, and effects of pharmaceuticals and personal care products in aquatic environments. *J. Hazard. Mater.* **2022**, *424*, 127284. https://doi.org/10.1016/j.jhazmat.2021.127284.
6. Chopra, S.; Kumar, D. Ibuprofen as an emerging organic contaminant in environment, distribution and remediation. *Heliyon* **2020**, *6*, e04087. https://doi.org/10.1016/j.heliyon.2020.e04087.
7. Żur, J.; Piński, A.; Marchlewicz, A.; Hupert-Kocurek, K.; Wojcieszyńska, D.; Guzik, U. Organic micropollutants paracetamol and ibuprofen—Toxicity, biodegradation, and genetic background of their utilization by bacteria. *Environ. Sci. Pollut. Res.* **2011**, *25*, 21498–21524.
8. He, C.; Tang, C.; Oh, W. Da Reinforced degradation of ibuprofen with MnCo2O4/FCNTs nanocatalyst as peroxymonosulfate activator: Performance and mechanism. *J. Environ. Chem. Eng.* **2022**, *10*, 107874. https://doi.org/10.1016/j.jece.2022.107874.
9. Paxéus, N.; Bester, K.; Haitham, E.T. Temporal variations and trends in loads of commonly used pharmaceuticals to large wastewater treatment plants in Sweden, a case study (Ryaverket). *Water Sci. Technol.* **2016**, *73*, 3049–3056. https://doi.org/10.2166/wst.2016.179.
10. Kudlek, E. Decomposition of contaminants of emerging concern in advanced oxidation processes. *Water* **2018**, *10*, 955. https://doi.org/10.3390/w10070955.
11. Jabeen, S.; Khan, M.S.; Khattak, R.; Zekker, I.; Burlakovs, J.; Rubin, S.S.; Ghangrekar, M.M.; Kallistova, A.; Pimenov, N.; Zahoor, M.; et al. Palladium-Supported Zirconia-Based Catalytic Degradation of Rhodamine-B Dye From Wastewater. *Water* **2021**, *13*, 1522.
12. Lee, J.; Von Gunten, U.; Kim, J.H. Persulfate-Based Advanced Oxidation: Critical Assessment of Opportunities and Roadblocks. *Environ. Sci. Technol.* **2020**, *54*, 3064–3081. https://doi.org/10.1021/acs.est.9b07082.
13. Yang, T.; Yu, D.; Wang, D.; Yang, T.; Li, Z.; Wu, M.; Petru, M.; Crittenden, J. Accelerating Fe (III)/Fe (II) cycle via Fe (II) substitution for enhancing Fenton-like performance of Fe-MOFs. *Appl. Catal. B Environ.* **2021**, *286*, 119859. https://doi.org/10.1016/j.apcatb.2020.119859.
14. Hu, Q.; Xu, L.; Fu, K.; Zhu, F.; Yang, T.; Yang, T.; Luo, J.; Wu, M.; Yu, D. Ultrastable MOF-based foams for versatile applications. *Nano Res.* **2022**, *15*, 2961–2970. https://doi.org/10.1007/s12274-021-3918-6.
15. Yu, D.; Wang, L.; Yang, T.; Yang, G.; Wang, D.; Ni, H.; Wu, M. Tuning Lewis acidity of iron-based metal-organic frameworks for enhanced catalytic ozonation. *Chem. Eng. J.* **2021**, *404*, 127075. https://doi.org/10.1016/j.cej.2020.127075.
16. Hu, Q.; Zhang, M.; Xu, L.; Wang, S.; Yang, T.; Wu, M.; Lu, W.; Li, Y.; Yu, D. Unraveling timescale-dependent Fe-MOFs crystal evolution for catalytic ozonation reactivity modulation. *J. Hazard. Mater.* **2022**, *431*, 128575. https://doi.org/10.1016/j.jhazmat.2022.128575.
17. Grzegórska, A.; Wysocka, I.; Głuchowski, P.; Ryl, J.; Karczewski, J.; Zielińska-Jurek, A. Novel composite of Zn/Ti-layered double hydroxide coupled with MXene for the efficient photocatalytic degradation of pharmaceuticals. *Chemosphere* **2022**, *308*, 136191. https://doi.org/10.1016/j.chemosphere.2022.136191.
18. Kowalkińska, M.; Fiszka Borzyszkowska, A.; Grzegórska, A.; Karczewski, J.; Głuchowski, P.; Łapiński, M.; Sawczak, M.; Zielińska-Jurek, A. Pilot-Scale Studies of WO3/S-Doped g-C3N4 Heterojunction toward Photocatalytic NOx Removal. *Materials* **2022**, *15*, 633.
19. Ameta, R.; Chohadia, A.K.; Jain, A.; Punjabi, P.B. In *Fenton and Photo-Fenton Processes*; Academic Press: Cambridge, MA, USA, **2018**; pp. 49–87. ISBN 9780128105252.
20. Yang, D.; Gopal, R.A.; Lkhagvaa, T.; Choi, D. Oxidizing agent impacting on growth of ZnO tetrapod nanostructures and its characterization. *Environ. Res.* **2021**, *197*, 111032. https://doi.org/10.1016/j.envres.2021.111032.
21. Vandamar Poonguzhali, R.; Ranjith Kumar, E.; Sumithra, M.G.; Arunadevi, N.; Rahale, C.S.; Munshi, A.M.; Mersal, G.A.M.; El-Metwaly, N.M. Natural citric acid (lemon juice) assisted synthesis of ZnO nanostructures: Evaluation of phase composition, morphology, optical and thermal properties. *Ceram. Int.* **2021**, *47*, 23110–23115. https://doi.org/10.1016/j.ceramint.2021.05.024.
22. Wang, J.; Chen, R.; Xiang, L.; Komarneni, S. Synthesis, properties and applications of ZnO nanomaterials with oxygen vacancies: A review. *Ceram. Int.* **2018**, *44*, 7357–7377. https://doi.org/10.1016/j.ceramint.2018.02.013.
23. Kouhail, M.; El Ahmadi, Z.; Benayada, A. Effect of Ag, Ca, and Fe on photocatalytic activity of ZnO nanoparticles to remove textile dyes under sunlight irradiation. *React. Kinet. Mech. Catal.* **2022**, *135*, 169–182. https://doi.org/10.1007/s11144-021-02061-1.

24. Fernandes, A.; Makoś, P.; Wang, Z.; Boczkaj, G. Synergistic effect of TiO2 photocatalytic advanced oxidation processes in the treatment of refinery effluents. *Chem. Eng. J.* **2020**, *391*, 123488. https://doi.org/10.1016/j.cej.2019.123488.
25. Mohamed, M.A.; Abd Mutalib, M.; Hir, Z.A.M.;Zain, M.F.M.; Mohamad, A.B.; Minggu, L.J.; Awang, N.A.; Salleh, W.N.W. An overview on cellulose-based material in tailoring bio-hybrid nanostructured photocatalysts for water treatment and renewable energy applications. *Int. J. Biol. Macromol.* **2017**, *103*, 1232–1256. https://doi.org/10.1016/j.ijbiomac.2017.05.181.
26. Rana, A.; Sudhaik, A.; Raizada, P.; Khan, A.A.P.; Van Le, Q.; Singh, A.; Selvasembian, R.; Nadda, A.; Singh, P. An Overview on Cellulose-Supported Semiconductor Photocatalysts for Water Purification; Springer International Publishing: New York, NY, USA, 2021; Volume 6.
27. Abdalkarim, S.Y.H.; Yu, H.Y.; Wang, C.; Huang, L.X.; Yao, J. Green synthesis of sheet-like cellulose nanocrystal–zinc oxide nanohybrids with multifunctional performance through one-step hydrothermal method. *Cellulose* **2018**, 25, 6433–6446. https://doi.org/10.1007/s10570-018-2011-0.
28. Nasiri Khalil Abad, S.; Mozammel, M.; Moghaddam, J.; Mostafaei, A.; Chmielus, M. Highly porous, flexible and robust cellulose acetate/Au/ZnO as a hybrid photocatalyst. *Appl. Surf. Sci.* **2020**, *526*, 146237. https://doi.org/10.1016/j.apsusc.2020.146237.
29. Tamaddon, F.; Mosslemin, M.H.; Asadipour, A.; Gharaghani, M.A.; Nasiri, A. Microwave-assisted preparation of $ZnFe_2O_4$@methyl cellulose as a new nano-biomagnetic photocatalyst for photodegradation of metronidazole. *Int. J. Biol. Macromol.* **2020**, *154*, 1036–1049. https://doi.org/10.1016/j.ijbiomac.2020.03.069.
30. Gesesse, G.D.; Gomis-Berenguer, A.; Barthe, M.F.; Ania, C.O. On the analysis of diffuse reflectance measurements to estimate the optical properties of amorphous porous carbons and semiconductor/carbon catalysts. *J. Photochem. Photobiol. A Chem.* **2020**, *398*, 112622. https://doi.org/10.1016/j.jphotochem.2020.112622.
31. Sakib, A.A.M.; Masum, S.M.; Hoinkis, J.; Islam, R.; Molla, M.A.I. Synthesis of CuO/ZnO nanocomposites and their application in photodegradation of toxic textile dye. *J. Compos. Sci.* **2019**, *3*, 91. https://doi.org/10.3390/jcs3030091.
32. Lamaming, J.; Hashim, R.; Sulaiman, O.; Leh, C.P.; Sugimoto, T.; Nordin, N.A. Cellulose nanocrystals isolated from oil palm trunk. *Carbohydr. Polym.* **2015**, *127*, 202–208. https://doi.org/10.1016/j.carbpol.2015.03.043.
33. Chieng, B.W.; Lee, S.H.; Ibrahim, N.A.; Then, Y.Y.; Loo, Y.Y. Isolation and characterization of cellulose nanocrystals from oil palm mesocarp fiber. *Polymers* **2017**, *9*, 355. https://doi.org/10.3390/polym9080355.
34. Cui, X.; Honda, T.; Asoh, T.A.; Uyama, H. Cellulose modified by citric acid reinforced polypropylene resin as fillers. *Carbohydr. Polym.* **2020**, *230*, 115662. https://doi.org/10.1016/j.carbpol.2019.115662.
35. Basnet, P.; Samanta, D.; Inakhunbi Chanu, T.; Mukherjee, J.; Chatterjee, S. Assessment of synthesis approaches for tuning the photocatalytic property of ZnO nanoparticles. *SN Appl. Sci.* **2019**, *1*, 633. https://doi.org/10.1007/s42452-019-0642-x.
36. Su, X.; Zhao, X.; Cui, C.; Xi, N.; Zhang, X.L.; Liu, H.; Yu, X.; Sang, Y. Influence of Wurtzite ZnO Morphology on Piezophototronic Effect in Photocatalysis. *Catalysts* **2022**, *12*, 946 https://doi.org/10.3390/catal12090946.
37. Smith, M.; Scudiero, L.; Espinal, J.; McEwen, J.S.; Garcia-Perez, M. Improving the deconvolution and interpretation of XPS spectra from chars by ab initio calculations. *Carbon N. Y.* **2016**, *110*, 155–171. https://doi.org/10.1016/j.carbon.2016.09.012.
38. Bu, Y.; Chen, Z.; Li, W. Using electrochemical methods to study the promotion mechanism of the photoelectric conversion performance of Ag-modified mesoporous g-C3N4 heterojunction material. *Appl. Catal. B Environ.* **2014**, *144*, 622–630. https://doi.org/10.1016/j.apcatb.2013.07.066.
39. Khalaf, S.; Shoqeir, J.H.; Lelario, F.; Bufo, S.A.; Karaman, R.; Scrano, L. TiO_2 and Active Coated Glass Photodegradation of Ibuprofen. *Catalysts* **2020**, *10*, 560.
40. Rastkari, N.; Eslami, A.; Nasseri, S.; Piroti, E.; Asadi, A. Optimizing parameters on nanophotocatalytic degradation of ibuprofen using UVC/ZnO processes by response surface methodology. *Pol. J. Environ. Stud.* **2017**, *26*, 785–794. https://doi.org/10.15244/pjoes/64931.
41. Jallouli, N.; Pastrana-Martínez, L.M.; Ribeiro, A.R.; Moreira, N.F.F.; Faria, J.L.; Hentati, O.; Silva, A.M.T.; Ksibi, M. Heterogeneous photocatalytic degradation of ibuprofen in ultrapure water, municipal and pharmaceutical industry wastewaters using a TiO2/UV-LED system. *Chem. Eng. J.* **2018**, *334*, 976–984. https://doi.org/10.1016/j.cej.2017.10.045.
42. Miranda, M.O.; Cabral Cavalcanti, W.E.; Barbosa, F.F.; Antonio De Sousa, J.; Ivan Da Silva, F.; Pergher, S.B.C.; Braga, T.P. Photocatalytic degradation of ibuprofen using titanium oxide: Insights into the mechanism and preferential attack of radicals. *RSC Adv.* **2021**, *11*, 27720–27733. https://doi.org/10.1039/d1ra04340d.
43. Sá, A.S.; Feitosa, R.P.; Honório, L.; Peña-Garcia, R.; Almeida, L.C.; Dias, J.S.; Brazuna, L.P.; Tabuti, T.G.; Triboni, E.R.; Osajima, J.A.; et al. A brief photocatalytic study of zno containing cerium towards ibuprofen degradation. *Materials* **2021**, *14*, 5891. https://doi.org/10.3390/ma14195891.
44. Arthur, R.B.; Bonin, J.L.; Ardill, L.P.; Rourk, E.J.; Patterson, H.H.; Stemmler, E.A. Photocatalytic degradation of ibuprofen over BiOCl nanosheets with identification of intermediates. *J. Hazard. Mater.* **2018**, *358*, 1–9. https://doi.org/10.1016/j.jhazmat.2018.06.018.
45. Shibu, M.C.; Benoy, M.D.; Shanavas, S.; Haija, M.A.; Duraimurugan, J.; Kumar, G.S.; Ahamad, T.; Maadeswaran, P.; Van Le, Q. White LED active α-Fe2O3/rGO photocatalytic nanocomposite for an effective degradation of tetracycline and ibuprofen molecules. *Environ. Res.* **2022**, *212*, 113301. https://doi.org/10.1016/j.envres.2022.113301.
46. Rosman, N.; Norharyati Wan Salleh, W.; Aqilah Mohd Razali, N.; Nurain Ahmad, S.Z.; Hafiza Ismail, N.; Aziz, F.; Harun, Z.; Fauzi Ismail, A.; Yusof, N. Ibuprofen removal through photocatalytic filtration using antifouling PVDF- ZnO/Ag2CO3/Ag2O nanocomposite membrane. *Mater. Today Proc.* **2019**, *42*, 69–74. https://doi.org/10.1016/j.matpr.2020.09.476.

47. da Luz, V.C.; Bazoti, S.F.; Behling, L.; Dalla Rosa, C.; Pasquali, G.D.L. Enhanced UV Direct Photolysis and UV/H2O2 for Oxidation of Triclosan and Ibuprofen in Synthetic Effluent: An Experimental Study. *Water Air Soil Pollut.* **2022**, *233*, 126. https://doi.org/10.1007/s11270-022-05583-z.
48. Behnajady, M.A.; Modirshahla, N. Evaluation of Electrical Energy Per Order (EEo) with Kinetic modeling on photooxidative degradation of C.I. Acid Orange 7 in a tubular continuous-flow photoreactor. *Ind. Eng. Chem. Res.* **2006**, *45*, 553–557. https://doi.org/10.1016/j.chemosphere.2005.05.027.
49. Wang, B.; Li, L.; Chen, J.; Duan, C.; Song, J.; Wang, R.; Zhang, B. Synthesis of BiOCl0. 5I0. 5/TiO_2 heterojunctions with enhanced visible-light photocatalytic properties. *J. Nano. Res. Vol.* **2018**, *20*, 175.
50. Chen, X.; Wu, Z.; Liu, D.; Gao, Z. Preparation of ZnO Photocatalyst for the Efficient and Rapid Photocatalytic Degradation of Azo Dyes. *Nanoscale Res. Lett.* **2017**, *12*, 4–13. https://doi.org/10.1186/s11671-017-1904-4.
51. Shiraishi, Y.; Ueda, Y.; Soramoto, A.; Hinokuma, S.; Hirai, T. Photocatalytic hydrogen peroxide splitting on metal-free powders assisted by phosphoric acid as a stabilizer. *Nat. Commun.* **2020**, *11*, 3386. https://doi.org/10.1038/s41467-020-17216-2.
52. Sahel, K.; Elsellami, L.; Mirali, I.; Dappozze, F.; Bouhent, M.; Guillard, C. Hydrogen peroxide and photocatalysis. *Appl. Catal. B Environ.* **2016**, *188*, 106–112. https://doi.org/10.1016/j.apcatb.2015.12.044.
53. Gao, X.; Zhang, S.; Liu, J.; Xu, S.; Li, Z. Enhanced active oxidative species generation over Fe-doped defective TiO2nanosheets for boosted photodegradation. *RSC Adv.* **2020**, *10*, 40619–40624. https://doi.org/10.1039/d0ra08116g.
54. Yu, H.Y.; Chen, G.Y.; Wang, Y.B.; Yao, J.M. A facile one-pot route for preparing cellulose nanocrystal/zinc oxide nanohybrids with high antibacterial and photocatalytic activity. *Cellulose* **2015**, *22*, 261–273. https://doi.org/10.1007/s10570-014-0491-0.
55. Ju, X.; Bowden, M.; Brown, E.E.; Zhang, X. An improved X-ray diffraction method for cellulose crystallinity measurement. *Carbohydr. Polym.* **2015**, *123*, 476–481. https://doi.org/10.1016/j.carbpol.2014.12.071.